INTERNATIONAL JOURNAL FOR NUMERICAL METHODS IN ENGINEERING

Int. J. Numer. Meth. Engng 2002; **00**:1–16 *Prepared using* nmeauth.cls *[Version: 2000/01/19 v2.0]*

Mesh independent p-orthotropic enrichment using the generalized finite element method

C. A. Duarte[1†*] and I. Babuška[2‡]

[1] *Universidade de São Paulo, EESC, Dep. de Estruturas, Av. Trabalhador SãoCarlense 400, São Carlos, SP, 13566-590, Brazil*

[2] *TICAM, The University of Texas at Austin, Austin, TX, 78712, USA*

SUMMARY

This paper is aimed at presenting a simple and yet effective procedure to implement a mesh independent p-orthotropic enrichment in the generalized finite element method. The procedure is based on the observation that shape functions used in the GFEM can be constructed from polynomials defined in any coordinate system regardless of the underlying mesh or type of element used. Numerical examples where the solution possesses boundary or internal layers are solved on coarse tetrahedral meshes with isotropic and the proposed p-orthotropic enrichment. Copyright © 2002 John Wiley & Sons, Ltd.

*Correspondence to: Universidade de São Paulo, EESC, Dep. de Estruturas, Av. Trabalhador SãoCarlense 400, São Carlos, SP, 13566-590, Brazil

†E-mail: armando@sc.usp.br Fax: (55)(16) 273-9482 Ph: (55)(16) 273-9455

‡E-mail: babuska@ticam.utexas.edu

Contract/grant sponsor: Sandia National Laboratories (C. A. Duarte); contract/grant number: BE 5367

Contract/grant sponsor: Office of Naval Research (I. Babuška); contract/grant number: N00014-99-1-0724

Received October 2001

Accepted 23 January 2002

KEY WORDS: Meshless; Meshfree; Generalized finite element method; Partition of unity method; *Hp*-cloud method; *P*-enrichment

1. INTRODUCTION

There are many important practical situations where the solution of a boundary-value problem has a very strong gradient in one direction but is relatively flat in others. This is the case, for example, in problems where boundary or internal layers occur. One very efficient approach to solve this class of problems is to use p-orthotropic approximations, that is, approximations that have different polynomial orders associated with each enrichment direction. This technique is well-known in the finite element community, but is infrequently used, mainly for practical reasons. In the finite element method the analyst must know *a-priori* the preferential directions of the solution and build the finite element mesh accordingly. However, in most practical cases, the geometry of the domain or the use of automatic mesh generators, precludes the construction of a finite element mesh along these directions. This constraint is inherent to the FEM and forces the use of isotropic approximations to solve this class of problems. The partition of unity framework used in the generalized finite element method (GFEM) [5, 6, 7, 11, 10, 13, 14, 9, 3] provides much more opportunities to efficiently solve this class of problems. The procedure proposed here is based on the observation that GFEM shape functions can be constructed from polynomials defined in any coordinate system. This allows the construction of shape functions of prescribed polynomial order along any given direction, regardless of the underlying mesh, type of element used or complexity of the geometry of the domain. The procedure presented is an extension of the one proposed by Duarte [8] in the framework of the *hp* cloud method.

Following this introduction, the construction of mesh independent p-orthotropic GFEM shape functions is presented in Section 2. Numerical examples demonstrating the effectiveness of the proposed approach are given in Section 3. Finally, in Section 4, the conclusions are outlined.

2. MESH INDEPENDENT P-ORTHOTROPIC APPROXIMATIONS

Let the functions $\varphi_\alpha,\ \alpha = 1,\dots,N$, denote a linear finite element partition of unity with supports ω_α (often called *clouds*). Here, N is the number of vertex nodes in the finite element mesh and ω_α is the union of the finite elements sharing the vertex node $\boldsymbol{x}_\alpha$.

Let $\chi_\alpha(\omega_\alpha) = \text{span}\{L_{i\alpha}\}_{i\in\mathcal{I}(\alpha)}$ denote local spaces defined on $\omega_\alpha,\ \alpha = 1,\dots,N$, where $\mathcal{I}(\alpha),\ \alpha = 1,\dots,N$, are index sets and $L_{i\alpha}$ denotes local approximation functions defined over the cloud ω_α.

The generalized finite element shape functions associated with a vertex node $\boldsymbol{x}_\alpha$ are defined by

$$\phi_i^\alpha = \varphi_\alpha L_{i\alpha},\ i \in \mathcal{I}(\alpha) \qquad \text{(no sum on } \alpha) \tag{1}$$

Details on the formulation of the GFEM can be found in, e.g., [6, 7, 11, 13]

Let us consider the case in which the functions $\{L_{i\alpha}\}_{i\in\mathcal{I}(\alpha)}$ are polynomials defined as follows

$$L_{i\alpha}(\boldsymbol{x}) = \widehat{L}_i \circ \mathbf{T}_\alpha^{-1}(\boldsymbol{x})$$

where:

$\widehat{\mathcal{L}}(\widehat{\omega}) := \{\widehat{L}_i\}_{i\in\mathcal{I}}$, are polynomials defined in a Cartesian system (ξ,η,ζ) and $\widehat{\omega}$ is the unit sphere

$$\widehat{\omega} := \{\boldsymbol{\eta} \in \mathbb{R}^3 : |\boldsymbol{\eta}|_{\mathbb{R}^3} \leq 1\};$$

$\mathbf{T}_\alpha^{-1}$ is a mapping from the global Cartesian coordinate system to a nodal Cartesian system given by

$$\mathbf{T}_\alpha^{-1} : \boldsymbol{x} = (x, y, z) \to \boldsymbol{\xi} = (\xi, \eta, \zeta)$$

$$\boldsymbol{\xi} = \mathbf{R}_\alpha^{-1}(\boldsymbol{x} - \boldsymbol{x}_\alpha)/h_\alpha$$

where $\mathbf{R}_\alpha^{-1} \in I\!R^3 \times I\!R^3$, with rows given by the base vectors of the coordinate system (ξ, η, ζ) written with respect of the base vectors of the coordinate system (x, y, z) and h_α is taken as the diameter of the largest element connected to node $\boldsymbol{x}_\alpha$.

The coordinate system (ξ, η, ζ) is illustrated in Figure 1. Note that the transformations $\mathbf{T}_\alpha^{-1},\ \alpha = 1, \ldots, N$, do not depend on the partition of unity (in this case a finite element mesh). Also, from the definition of $\mathbf{T}_\alpha^{-1}, \alpha = 1, \ldots, N$, we have that if $\boldsymbol{x} \in \omega_\alpha$ then $\boldsymbol{\xi} = \mathbf{T}_\alpha^{-1}(\boldsymbol{x}) \in \widehat{\omega}$ since $|\boldsymbol{x} - \boldsymbol{x}_\alpha|_{I\!R^3}/h_\alpha \leq 1$ and $\mathbf{R}_\alpha^{-1},\ \alpha = 1, \ldots, N$, represent rotations.

[Figure 1 about here.]

2.1. Local approximation for p-orthotropic enrichment

In this section, details about the elements of the set $\widehat{\mathcal{L}}(\widehat{\omega})$ used in our computations are provided. This set is composed of monomials of degree (p_ξ, p_η, p_ζ) along the local (nodal) Cartesian directions ξ, η, ζ, respectively.

In the case of isotropic enrichment, i.e., $p_\xi = p_\eta = p_\zeta = p$, the set $\widehat{\mathcal{L}}(\widehat{\omega})$ is taken from the Pascal triangle [12] and the notation $\widehat{\mathcal{L}}_p(\widehat{\omega})$ is used.

$$\widehat{\mathcal{L}}_p(\widehat{\omega}) = Q'_p(\widehat{\omega}) := \{\xi^i \eta^j \zeta^k : 0 \leq i + j + k \leq p,\ i, j, k = 0, \ldots, p,\ (\xi, \eta, \zeta) \in \widehat{\omega}\}$$

Let the set of tensor product polynomials of degree (p_ξ, p_η, p_ζ) be denoted by

$$Q_{(p_\xi, p_\eta, p_\zeta)}(\widehat{\omega}) := \{\xi^i \eta^j \zeta^k : 0 \leq i \leq p_\xi,\ 0 \leq j \leq p_\eta,\ 0 \leq k \leq p_\zeta,\ (\xi, \eta, \zeta) \in \widehat{\omega}\}$$

In the general case of orthotropic nodal enrichment, the following set of polynomials is use

$$\widehat{\mathcal{L}}_{(p_\xi,p_\eta,p_\zeta)}(\widehat{\omega}) := Q'_{\bar{p}}(\widehat{\omega}) \cap Q_{(p_\xi,p_\eta,p_\zeta)}(\widehat{\omega})$$

where $\bar{p} = \max\{p_\xi, p_\eta, p_\zeta\}$.

This set is complete of degree (p_ξ, p_η, p_ζ) in the directions ξ, η, ζ, respectively, while having less elements than the set $Q_{(p_\xi,p_\eta,p_\zeta)}$.

Let (p_1, p_2, p_3) denote the degree of the GFEM shape function as defined in (1). Then we have that $p_1 = p_\xi + 1,\ p_2 = p_\eta + 1,\ p_3 = p_\zeta + 1$ since the partition of unity is a linear polynomial (linear finite element shape functions). Examples of local approximations $\widehat{\mathcal{L}}$ are

(i) Linear basis in three-dimensional space

$$\widehat{\mathcal{L}}_{(p_\xi=p_\eta=p_\zeta=1)} = \{1, \xi, \eta, \zeta\}$$

The resulting GFEM shape functions are quadratic (and complete) in the directions (ξ, η, ζ), i.e., $p_1 = p_2 = p_3 = 2$.

(ii) Cubic basis in the direction ξ and quadratic in the direction η, i.e. $(p_\xi = 3,\ p_\eta = 2)$, in a two-dimensional space

$$\widehat{\mathcal{L}}_{(p_\xi=3,p_\eta=2)} = Q'_{\bar{p}=3} \cap Q_{(p_\xi=3,p_\eta=2)} = \{1, \xi, \xi^2, \xi^3, \eta, \xi\eta, \xi^2\eta, \xi\eta^2, \eta^2\}$$

In this case, the resulting GFEM shape functions are of degree $p_1 = 4,\ p_2 = 3$.

3. NUMERICAL EXPERIMENTS

3.1. Boundary layers

The solution of fluid flow problems and of plate- or shell-like structural models in solid mechanics generally contains the so-called boundary layers. These are rapidly varying

components of the solution that decay exponentially with respect to the distance from the boundary. As an illustration of this phenomenon, consider the plate-like structure depicted in Figure 2. The body is assumed to be linear elastic with Young's modulus $E = 2.1e11$ PA and Poisson's ratio $\nu = 0.3$. The dimensions L_x, L_y and d are taken as $L_x = L_y = \pi$ m and $d = 0.02$ m, respectively. A distributed load $q(x, y) = Q/2 \cos x$ PA is applied at the lower ($z = 0$) and upper ($z = d$) surfaces in the direction shown in the figure. The constant Q is taken as $Q = 10,000$. The surface $y = 0$ is free and symmetry boundary conditions are applied at the surfaces $x = 0,\ x = L_x$ and $y = L_y$ as indicated in Figure 2.

[Figure 2 about here.]

The solution of the Reissner-Mindlin plate model of the body shown in Figure 2 can represent well the 3-dimensional linear elasticity solution with appropriate modifications of the elastic constants [4, 15]. The Reissner-Mindlin solution can also approximate well the boundary layer behavior of the 3-dimensional solution. For the boundary conditions shown in Figure 2 *and* L_y *sufficiently large*, the shear stress component τ_{xz} computed from the solution of the Reissner-Mindlin model is given by [15, 1]

$$\tau_{xz} = -\frac{Q}{d^3}\left[d^2 + C_2 2\frac{D}{d}e^{-y} - C_4 d\gamma e^{-\frac{\gamma y}{d}}\right]\sin x \tag{2}$$

where

$$\begin{aligned}
\gamma &= \sqrt{12\kappa + d^2} \\
D &= \frac{Ed^3}{12(1-\nu^2)} \\
C_2 &= \frac{\kappa G \nu d^3}{Df} \\
C_4 &= \frac{2\kappa G \nu}{f}
\end{aligned}$$

$$
\begin{aligned}
f &= -2\kappa G + (1-\nu)\left[\kappa G - \frac{D}{d^3}(\gamma - d)^2\right] \\
G &= \frac{E}{2(1+\nu)}
\end{aligned}
$$

and κ is the shear correction factor.

The exponential terms in (2) causes the transversal shear stress τ_{xz} to have a high rate of change in the direction y near the free boundary, i.e., $y = 0$. This boundary layer behavior becomes stronger as the plate thickness decreases. However, in all other directions τ_{xz} is constant or a very smooth function. As a result, the approximation of this type of function using isotropic polynomials is far from optimal.

The problem of Figure 2 was solved using the GFEM with the hexahedral mesh of Figure 3 (top view). The mesh has 2, 18 and 1 element in the x-, y- and z-direction, respectively. The size of the elements decreases in geometric progression towards $y = 0$ with a geometric factor $g = 1./1.2$. The first layer of nodes at the free boundary, i.e., nodes located at $(x, 0, 0)$ and $(x, 0, d),\ 0 \leq x \leq L_x$, and the next layer of nodes are enriched to $(p_1 = 5, p_2 = 8, p_3 = 4)$ in the x-, y- and z-directions, respectively. The p-order of all other nodes are $(p_1 = 5, p_2 = 5, p_3 = 4)$ in the x-, y- and z-directions, respectively. The p-enrichment is done as described in Section 2 or in, e.g., [6]. The total number of equations for this discretization is 40,942 and we refer to it as the overkill discretization. The corresponding solution is taken as the reference solution in all subsequent computations in this section. The accuracy of this solution was investigated by comparing it with other solutions computed with a varying number of elements and degree of approximation. In all discretizations investigated, the computed value of τ_{zy} at $\boldsymbol{x} = (2.0, 0, d/2)$ were within 0.01% of each other.

[Figure 3 about here.]

Figure 4 shows point wise values of the shear stress component τ_{xz} along the segment $[2.0, y, d/2],\ 0 \leq y \leq L_y$, computed with the overkill discretization. The figure shows that the shear stress τ_{xz} varies very rapidly near the free edge of the thin-body ($y = 0$) as predicted by (2).

[Figure 4 about here.]

In this section, we investigate the effectiveness of the mesh independent p-orthotropic enrichment technique presented in Section 2 to model boundary layers in thin solids. We use the uniform tetrahedral mesh shown in Figure 5 and several p-enrichment strategies to analyze the problem of Figure 2. This mesh was generated by first creating a hexahedral mesh with 2, 20 and 1 element in the x-, y- and z-direction, respectively. Each element was then divided into 6 tetrahedral elements. This mesh is denoted by $2 \times 20 \times 1(*6)$.

A local coordinate system parallel to the xyz global coordinate system is defined at each node of the mesh. These nodal systems are used to build shape functions of prescribed polynomial orders in the directions of the local coordinate axes as described in the previous section. A representation of such nodal coordinate systems is shown in Figure 6. The grey level of each coordinate axis indicates the polynomial order of the nodal shape functions along that direction.

[Figure 5 about here.]

[Figure 6 about here.]

The modeling of thin solids like that of Figure 2 with the GFEM or the FEM brings the issue of shear locking. As the body becomes thin, the transverse shear strain becomes negligible. Low order solid elements based on a displacement formulation can not represent this state of

zero transverse shear strain and the finite element solution will be overly stiff. One remedy for this problem is to use elements of polynomial order $p \geq 4$ [2]. We adopt this approach in our computations.

Figure 7 shows the relative error

$$\mathcal{E}_r(w_p) = \left| \frac{w - w_p}{w} \right| \tag{3}$$

of the transversal displacement computed with the mesh of Figure 5 and GFEM shape functions of degree $(4, 4, 4)$. The relative error is computed along the segment $[2.0, y, d/2],\ 0 \leq y \leq L_y$, using the overkill solution. The maximum relative error is of only 0.144 %. This discretization is effective to model the transversal displacement because *it does not* exhibit the boundary layer behavior like the shear stress does [1]. However, this discretization is not appropriate to model the near boundary behavior of engineering quantities like the transversal shear stresses. Figure 8 shows the relative error

$$\mathcal{E}_r(\tau_{xz}^p) = \left| \frac{\tau_{xz} - \tau_{xz}^p}{\tau_{xz}} \right| \tag{4}$$

of the shear stress component τ_{xz} computed with the same discretization and along the same segment. The error at $y = 0$, which is the location of the maximum value of τ_{xz}, is of 43.49 %.

[Figure 7 about here.]

[Figure 8 about here.]

We investigate four sequences of p-enrichment on the tetrahedral mesh $2 \times 20 \times 1 (*6)$ with the goal of finding the best approach to model the boundary layer behavior of τ_{xz}. The sequences are the following:

Sequence 1: All nodes are enriched to $(p_1, p_2, 4),\ 4 \leq p_1, p_2 \leq 7$. This choice of enrichment is motivated by the fact that the dimension of the domain in the z-direction is much smaller than in the other directions.

Sequence 2: The first two layers of nodes at or near the free boundary, i.e., nodes located at $(x, 0, 0),\ (x, 0, d),\ (x, L_y/20, 0),\ (x, L_y/20, d),\ 0 \leq x \leq L_x$, are isotropically enriched to $(q, q, q),\ 4 \leq q \leq 8$. The p-order of all other nodes are kept at $(4, 4, 4)$.

This strategy of enrichment is based on the observation that the boundary layer effect is restricted to the region very close to the free boundary ($y = 0$). Away from there, the solution is very smooth (Cf. (2)). Note that the enrichment of the first two layers of nodes is equivalent to the enrichment of the first layer of elements. We chose to enrich isotropically to mimic the limitations of the finite element method on tetrahedral meshes. The performance of this sequence will give us a good estimate of the performance of the finite element method on this problem.

Sequence 3: In this sequence, like in the previous one, only the first two layers of nodes are enriched. However, here we use an orthotropic enrichment. The nodes at the first two layers are enriched to $(4, p_2, 4),\ 4 \leq p_2 \leq 8$, while all other nodes have degree $(4, 4, 4)$.

Sequence 4: This is exactly like the previous one except that only the first layer of nodes, i.e, nodes located at $(x, 0, 0),\ (x, 0, d),\ 0 \leq x \leq L_x$, are enriched to $(4, p_2, 4),\ 4 \leq p_2 \leq 8$, while all other nodes have degree $(4, 4, 4)$.

The performance of the above sequences of enrichment is measured by the convergence of the shear stress component τ_{xz} at $\boldsymbol{x} = (2.0, 0, d/2)$. We take

$$\tau_{xz}(2.0, 0, d/2) = 1.948e7,$$

computed with the overkill discretization, as the reference value.

Figure 9 shows the relative error (4) versus the number of degrees of freedom for Sequences 1-4. All four sequences show an exponential convergence of the shear stress at $\boldsymbol{x} = (2.0, 0, d/2)$. This is expected because of the regularity of the solution. Sequence 1 is the least effective. This indicates that enriching the nodes far from the boundary layer is not effective. Sequence 2, which we expect to represent the behavior of the finite element method on this mesh, is the second least effective strategy. This indicates that enriching the approximation in directions other than that of the boundary layer (as required by the FEM) is not effective. The most effective sequence is Sequence 4. This shows that the most effective strategy to model the boundary layer is simply to enrich the nodes at the boundary in the direction of the boundary layer. Figure 9 shows that, for the same number of degrees of freedom, the point wise error of the stress components in Sequence 4 can be up to one order of magnitude smaller than in Sequence 2.

[Figure 9 about here.]

[Table 1 about here.]

Figure 10 shows the point wise values of (4) along the segment $[2.0, y, d/2],\ 0 \leq y \leq L_y$, for discretization $2 \times 20 \times 1(*6)$ and p-order $(4, 4, 4)$ with and without enrichment of the nodes at the boundary layer. As mentioned previously, the discretization with p-order $(4, 4, 4)$ has a relative error on τ_{xz} of 43.49% at $(2.0, 0, d/2)$. The enrichment of the first layer of nodes reduces this error to just 1.83 %. These data are also available in Table I (Sequence 4 data). The enrichment of the first layer of nodes affects only the corresponding layer of elements which is of dimension $L_y/20 = 0.157$ in the y-direction. However, as can be observed in Figure

10, the beneficial effects of the enrichment extends beyond the first layer of elements.

[Figure 10 about here.]

Figures 11 and 12 are analogous to Figure 10 but for the case of tetrahedral meshes with $2 \times 30 \times 1(*6)$ and $2 \times 60 \times 1(*6)$ elements, respectively. The discretization $2 \times 30 \times 1(*6)$ with p-order $(4,4,4)$ has a relative on τ_{xz} of 27.45% at $(2.0, 0, d/2)$. The enrichment of the first layer of nodes to $(4,8,4)$ reduces this error to 0.12 %. The first layer of elements has dimension $L_y/30 = 0.105$ in the y-direction. Figure 11 shows that, as in the case of Figure 10, the reduction of the error in τ_{xz} extends beyond the first layer of elements. The effect of this enrichment can be observed up to about $y = 0.64$ (that is about the first 6 layers of elements).

[Figure 11 about here.]

[Figure 12 about here.]

3.2. Internal layer

Let us consider the following Neumann problem for the linear elasticity equations on $\Omega = \{(x,y,z) \in \mathbb{R}^3 \ : 0 < x < 10,\ 0 < y < 10,\ 0 < z < 0.1\}$

$$\begin{aligned} \sigma_{ij,j} + b_i &= 0 \qquad \text{in } \Omega \\ \sigma_{ij} &= D_{ijkl}\epsilon_{kl} \\ \epsilon_{ij} &= \frac{1}{2}(u_{i,j} + u_{j,i}) \\ \sigma_{ij} n_j &= T_i \qquad \text{on } \partial\Omega \end{aligned} \tag{5}$$

where D_{ijkl} is the tensor of elastic constants for a homogeneous isotropic material with Young's modulus $E = 1.0$ MPA and Poisson's ratio $\nu = 0.3$. The body forces, $b_i, i = 1,2,3$, and traction

components, $T_i, i = 1, 2, 3$, are such that the solution $\boldsymbol{u} = (u_1, u_2, u_3)$ is given by

$$u_1 = u_2 = u_3 = f(r) = exp\,(-\frac{4}{49}r^2 + \frac{8}{7}r) \tag{6}$$

where $r = \sqrt{(x+1)^2 + (y+1)^2}$. All the dimensions are in SI units.

The function $f(r)$ is analytic in Ω and has a large gradient in the r direction and is constant in the θ and z directions. Here, (r, θ, z) is a cylindrical coordinate system parallel to the global Cartesian system (x, y, z) with origin at $(-1, -1, 0)$. This function was chosen to investigate the performance of the p-orthotropic enrichment technique proposed in Section 2 to model internal layers. Figure 13 shows $f(r)$.

[Figure 13 about here.]

We solve the problem defined in (5) using the GFEM with shape functions as defined in the previous section. The mesh used to build the partition of unity is shown on Figure 14. It has $5 \times 5 \times 1(*6) = 150$ elements and does not take into account the behavior of the solution. Associated with each vertex node there is a Cartesian coordinate system with the directions ξ, η, ζ parallel to the directions r, θ, z, respectively. The cylindrical system (r, θ, z) is the same used to define function $f(r)$ in (6). The nodal Cartesian systems are illustrated in Figure 15. Note that, unlike in the previous problem, the orientation of the nodal coordinate systems used here varies from node to node.

[Figure 14 about here.]

[Figure 15 about here.]

Three sequences of enrichment are used. In the first case isotropic p-enrichment with $1 \leq p \leq 5$ is used. This is typically what must be used in the finite element method since

directional p-enrichment on tetrahedral meshes is almost impossible to be done in practice. The relative error in the energy norm as a function of the number of floating point operations (NFLOPS) for the numerical factorization of the stiffness matrix is shown in Figure 16.

The second and third sequences use p-orthotropic shape functions. The enrichment is done along the directions of the coordinate systems of the nodes. In the second sequence, $1 \leq p_1 \leq 7, p_2 = p_3 = 1$. In the third sequence, $1 \leq p_1 \leq 8, p_2 = 2, p_3 = 1$. The relative error in the energy norm for both sequences is shown in Figure 16. The effectiveness of p-orthotropic approximations can clearly be observed. The use of p-orthotropic enrichment made possible by the partition of unity framework used in the GFEM leads to quite substantial savings in terms of NFLOPS. For a given computational effort, the relative error in the energy norm for sequence two or three can be about one order of magnitude smaller than for sequence one (isotropic enrichment). However, it can be observed that the convergence rate of sequences 2 and 3 decreases for $p_1 \geq 4$, in the case of sequence 2, and $p_1 \geq 7$ in the case of sequence 3. Here, only the nodal direction ξ is enriched while the p-order in the other two directions are kept fixed. However, depending on the level of the discretization error, the direction ξ is not the optimal direction for enrichment, as can be observed in Figure 16. By optimal we mean the direction that gives the largest reduction in the discretization error for a given number of additional degrees of freedom. The optimal direction for enrichment can be found, for example, using the so-called directional a-posteriori error indicators.

[Figure 16 about here.]

4. CONCLUSIONS

In this paper, we propose a simple but very generic approach to implement directional p-enrichment in the GFEM. The resulting technique can be used in any dimension and with any type of element without modifications. This is in contrast with the classical finite element method where directional p-enrichment is coupled with the mesh and type of element used.

ACKNOWLEDGEMENTS

The support of this work by the Sandia National Laboratories (C. A. Duarte) under grant BE 5367 and by the Office of Naval Research (I. Babuška) under grant N00014-99-1-0724 is gratefully acknowledged.

REFERENCES

1. Arnold DN, Falk RS. Edge effects in the Reissner-Mindlin plate theory. In Noor AK, Belytschko T, Simo JC, editors, *Analytical and Computational Models of Shells*, pages 71–89. The American Society of Mechanical Engineers, 1989.
2. Babuška I, Li L. The problem of plate modeling: Theoretical and computational results. *Computer Methods in Applied Mechanics and Engineering*, 100:249–273, 1992.
3. Babuška I, Melenk JM. The partition of unity finite element method. *International Journal for Numerical Methods in Engineering*, 40:727–758, 1997.
4. Cho JR. An *hpq*-adaptive finite element method for hierarchical modeling of elastic structures. PhD dissertation, The University of Texas at Austin, December 1995. Austin, TX, USA.
5. Duarte CA, Babuška I, Oden JT. Generalized finite element methods for three dimensional structural mechanics problems. In Atluri SN, O'Donoghue PE, editors, *Modeling and Simulation Based Engineering*, volume I, pages 53–58. Tech Science Press, October 1998. Proceedings of the International Conference on Computational Engineering Science, Atlanta, GA, October 5-9, 1998.
6. Duarte CA, Babuška I, Oden JT. Generalized finite element methods for three dimensional structural mechanics problems. *Computers and Structures*, 77:215–232, 2000.

7. Duarte CA, Hamzeh ON, Liszka TJ, Tworzydlo WW. A generalized finite element method for the simulation of three-dimensional crack propagation. *Computer Methods in Applied Mechanics and Engineering*, 190:2227–2262, 2001.
8. Duarte CA. *The hp Cloud Method*. PhD dissertation, The University of Texas at Austin, December 1996. Austin, TX, USA.
9. Melenk JM, Babuška I. The partition of unity finite element method: Basic theory and applications. *Computer Methods in Applied Mechanics and Engineering*, 139:289–314, 1996.
10. Oden JT, Duarte CA, Zienkiewicz OC. A new cloud-based *hp* finite element method. Technical report, TICAM Report 96-55, The University of Texas at Austin, Austin, Texas, USA, December 1996.
11. Oden JT, Duarte CA, Zienkiewicz OC. A new cloud-based *hp* finite element method. *Computer Methods in Applied Mechanics and Engineering*, 153:117–126, 1998.
12. Oden JT, Reddy JN. *An Introduction to the Mathematical Theory of Finite Elements*. John Wiley and Sons, New York, 1976.
13. Strouboulis T, Babuška I, Copps K. The design and analysis of the generalized finite element method. *Computer Methods in Applied Mechanics and Engineering*, 81(1–3):43–69, 2000.
14. Strouboulis T, Copps K, Babuška I. The generalized finite element method: An example of its implementation and illustration of its performance. *International Journal for Numerical Methods in Engineering*, 47(8):1401–1417, 2000.
15. Szabó B, Babuška I. *Finite Element Analysis*. John Wiley and Sons, New York, 1991.

List of Figures

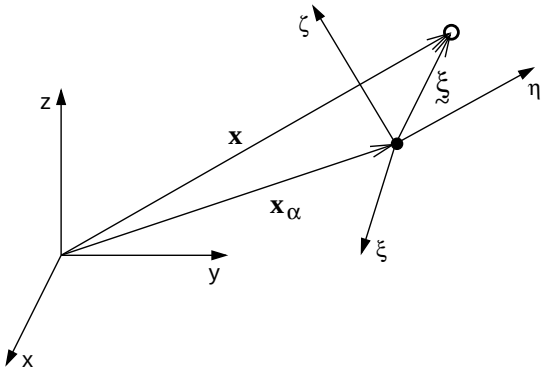

Figure 1. Coordinate system associated with a node $\boldsymbol{x}_\alpha$ of a finite element mesh.

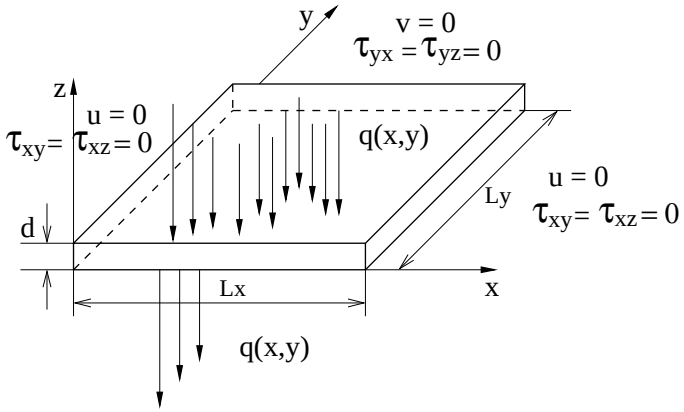

Figure 2. Boundary conditions for a plate-like structure.

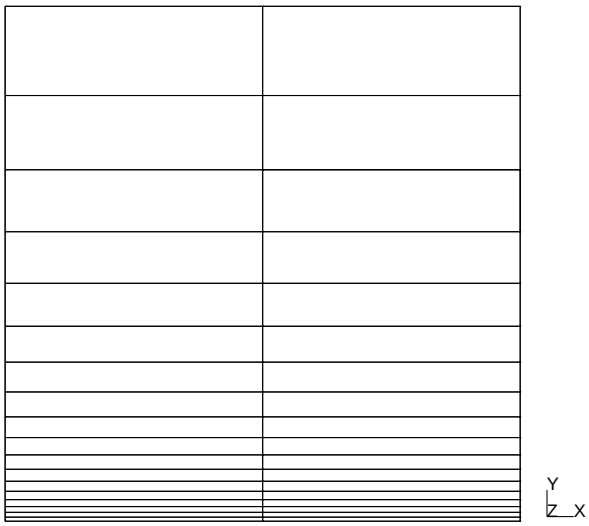

Figure 3. Hexahedral mesh used for overkill discretization (top view).

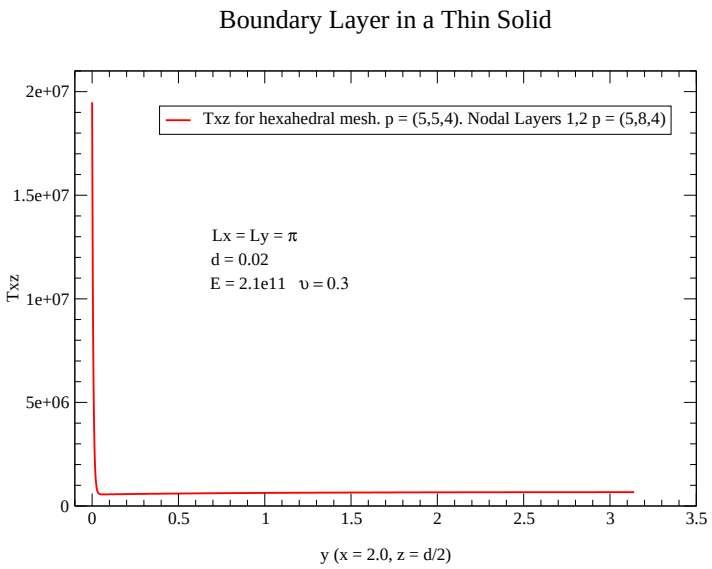

Figure 4. Boundary layer behavior of the shear stress component τ_{xz} near the free edge $y = 0$. The computation was done with the overkill discretization.

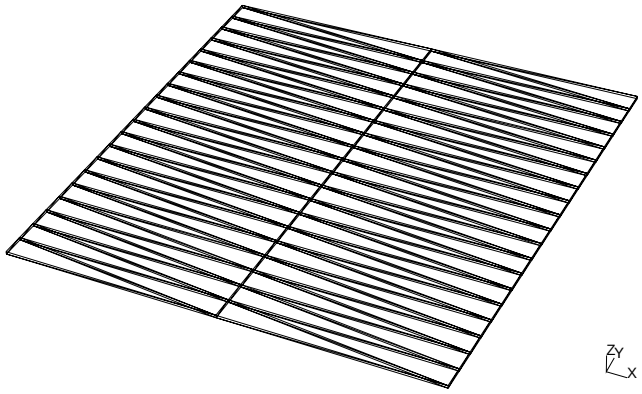

Figure 5. Uniform tetrahedral mesh $2 \times 20 \times 1(*6)$.

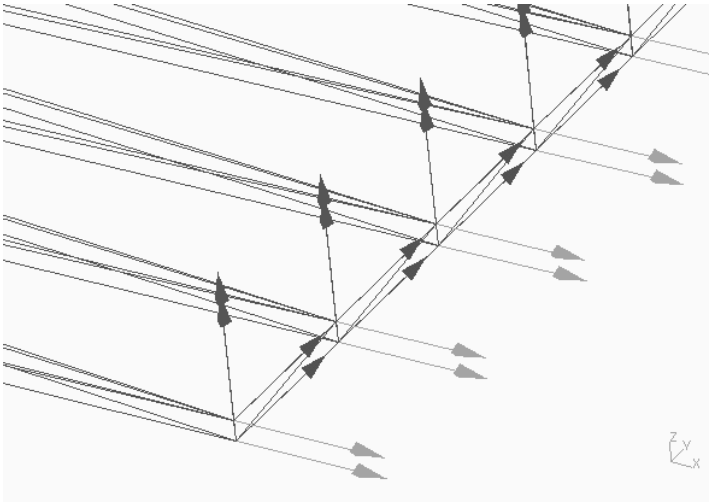

Figure 6. Coordinate system at nodes used to build p-orthotropic shape functions on a tetrahedral mesh.

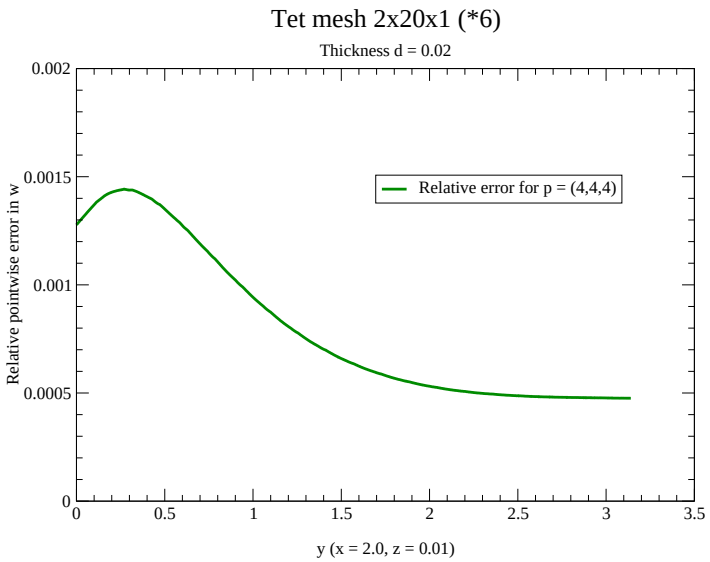

Figure 7. Relative point wise error in transversal displacement w for the mesh of Figure 5 and p-order $(4, 4, 4)$.

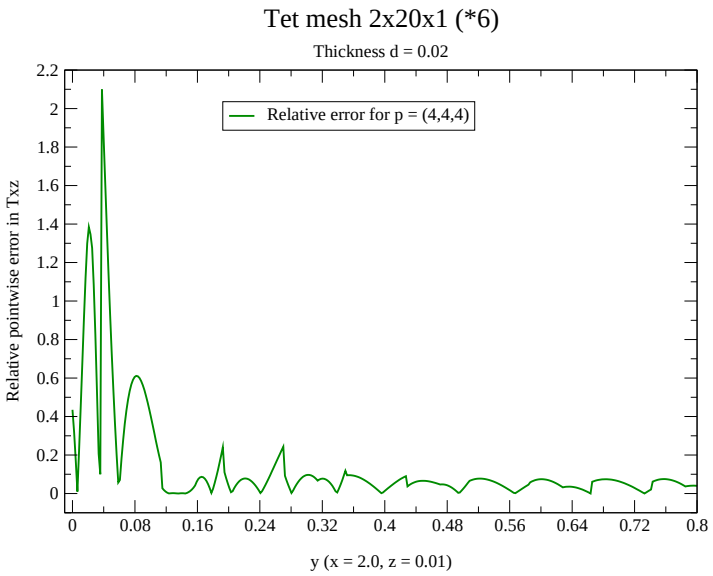

Figure 8. Relative point wise error in shear stress τ_{xz} for discretization of Figure 5 and p-order $(4, 4, 4)$.

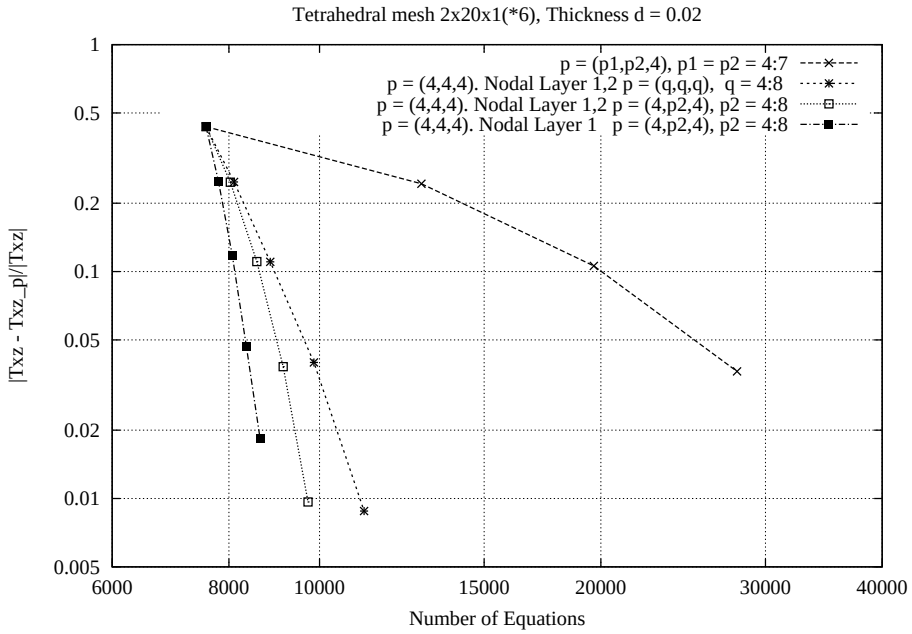

Figure 9. Convergence of τ_{xz} at $\boldsymbol{x} = (2.0, 0, d/2)$ for mesh $2 \times 20 \times 1(*6)$ and p-Sequences 1-4.

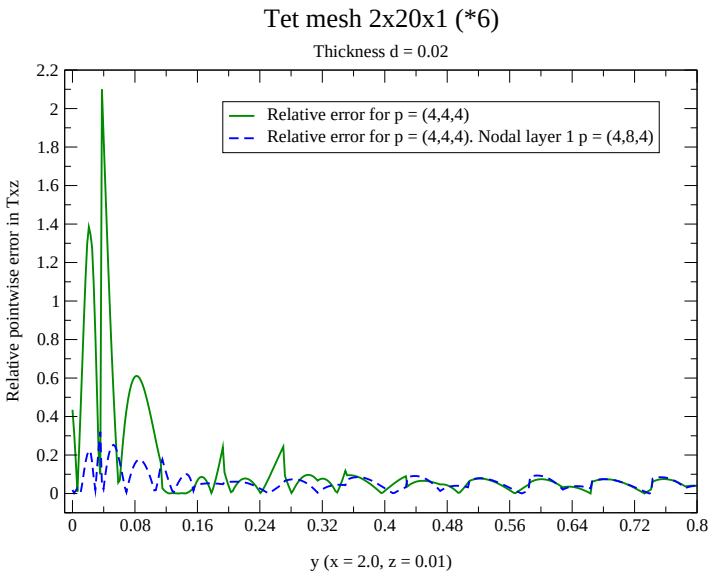

Figure 10. Relative point wise error in τ_{xz} for discretization $2 \times 20 \times 1(*6)$ and p-order $(4, 4, 4)$ with and without enrichment of the first layer of nodes.

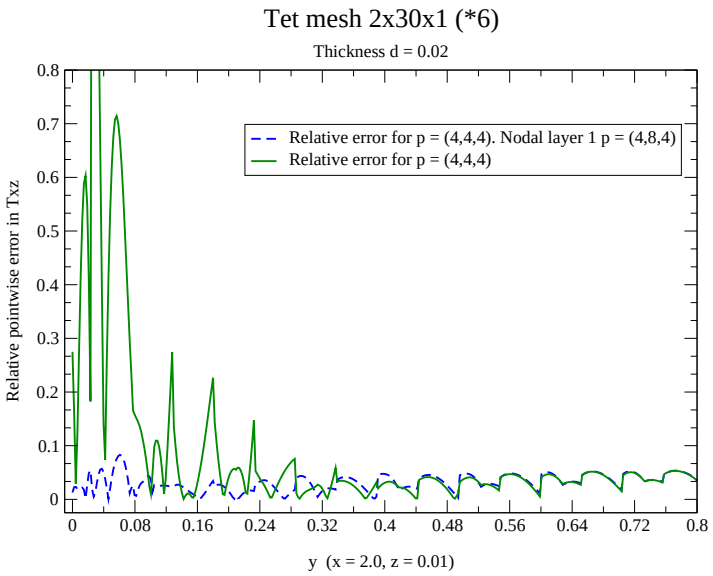

Figure 11. Relative point wise error in τ_{xz} for discretization $2 \times 30 \times 1(*6)$ and p-order $(4, 4, 4)$ with and without enrichment of the first layer of nodes.

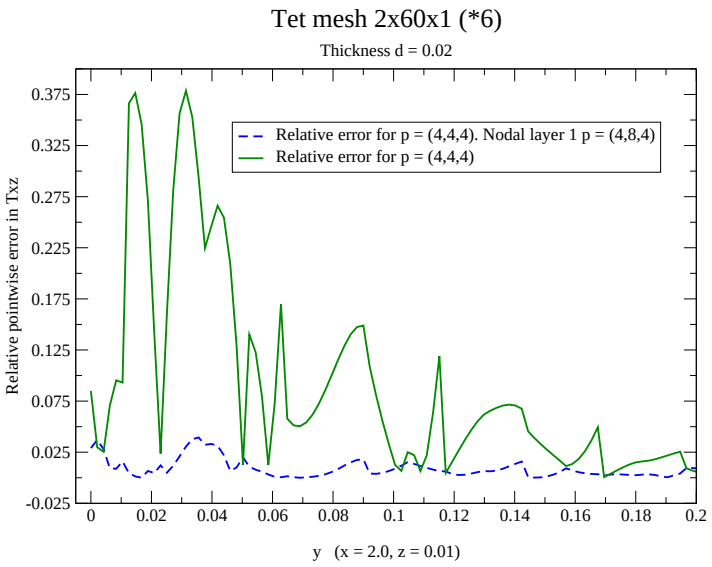

Figure 12. Relative point wise error in τ_{xz} for discretization $2 \times 60 \times 1(*6)$ and p-order $(4, 4, 4)$ with and without enrichment of the first layer of nodes.

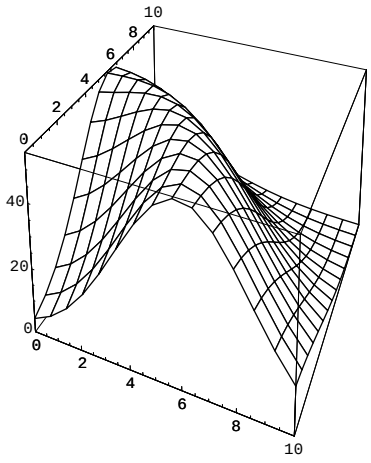

Figure 13. Function $f(r)$.

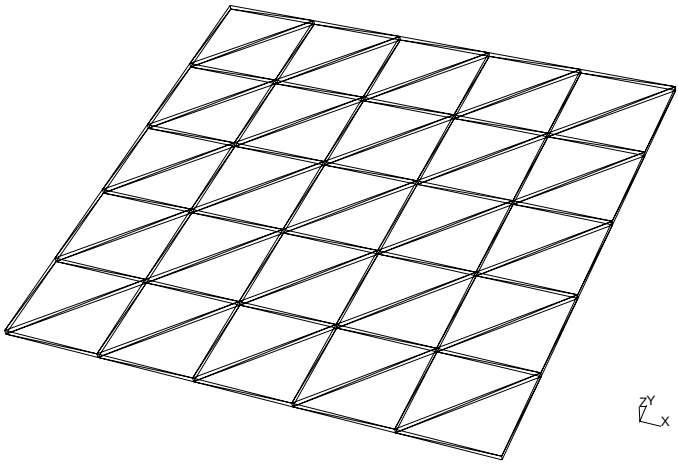

Figure 14. Tetrahedral mesh $5 \times 5 \times 1(*6)$ used to solve problem (5).

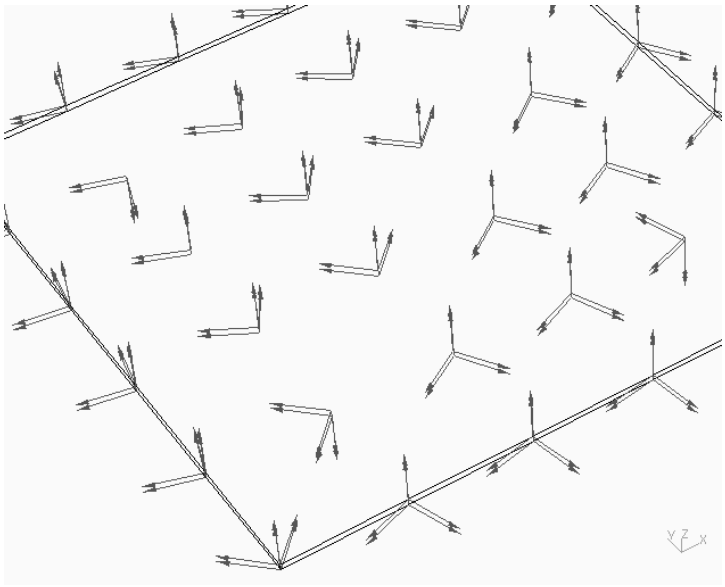

Figure 15. Coordinate system at nodes used to build p-orthotropic shape functions on a tetrahedral mesh. The coordinate systems are oriented along the coordinate lines of a cylindrical system parallel to the global system xyz and with origin at $(-1, -1, 0)$.

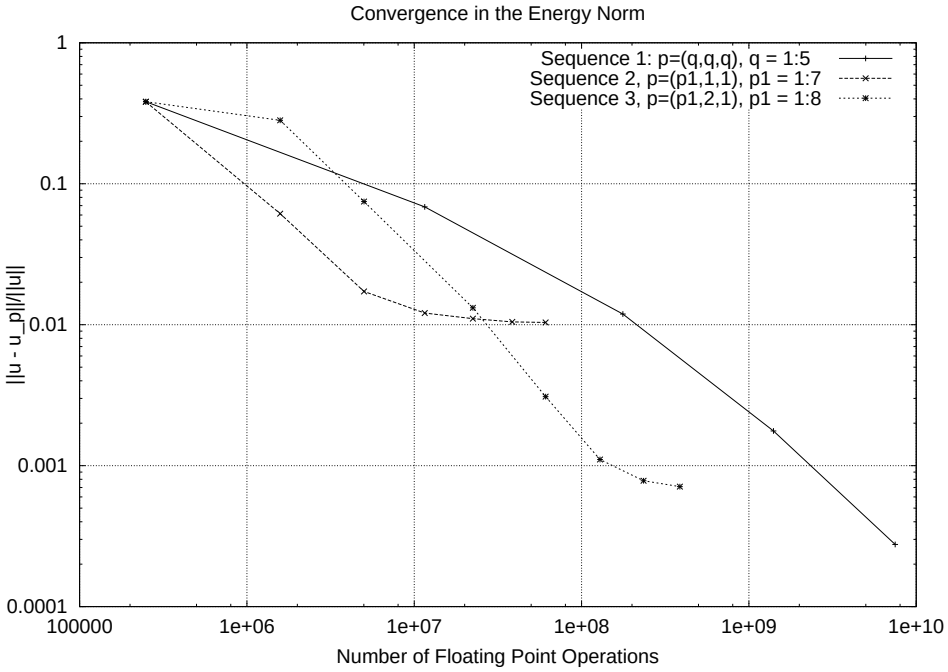

Figure 16. Convergence in the energy norm for isotropic and orthotropic p-enrichments.

List of Tables

Table I. Convergence of τ_{xz} for mesh $2\times20\times1(*6)$ and p-Sequences 1-4. Here, $\mathcal{E}_r(\tau^p_{xz}) = |\tau_{xz}-\tau^p_{xz}|/|\tau_{xz}|$ computed at $\boldsymbol{x} = (2.0, 0, d/2)$ and N_i is the number of degrees of freedom of Sequence i.

Sequence 1		Sequence 2		Sequence 3		Sequence 4	
N_1	$\mathcal{E}_r(\tau^p_{xz})$	N_2	$\mathcal{E}_r(\tau^p_{xz})$	N_3	$\mathcal{E}_r(\tau^p_{xz})$	N_4	$\mathcal{E}_r(\tau^p_{xz})$
7560	0.4349	7560	0.4349	7560	0.4349	7560	0.4349
12852	0.2436	8100	0.2482	8028	0.2476	7794	0.2502
19656	0.1058	8856	0.1103	8568	0.1106	8064	0.1182
27972	0.0363	9864	0.0398	9144	0.0381	8352	0.0466
		11160	0.0088	9720	0.0097	8640	0.0183